BOLETÍN DE LA SOCIEDAD ESPAÑOLA DE CERÁMICA Y VIDRIO XXX (2024) XXX–XXX

BOLETIN DE LA SOCIEDAD ESPAÑOLA DE
Cerámica y Vidrio
www.elsevier.es/bsecv

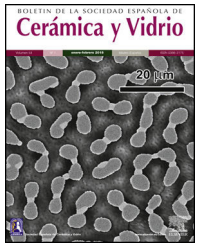

Original

Basic microstructural, mechanical, electrical and optical characterisation of $BaTiAl_6O_{12}$ ceramics

Daniel Drdlik[a,b,*], Vojtech Marak[a], Robert Klement[c], Pavel Tofel[a,d], Katarina Drdlikova[a], Hynek Hadraba[e], Zdenek Chlup[e]

[a] CEITEC BUT, Brno University of Technology, Purkynova 123, 612 00 Brno, Czech Republic
[b] Institute of Materials Science and Engineering, Brno University of Technology, Technicka 2, 616 00 Brno, Czech Republic
[c] FunGlass, Alexander Dubcek University of Trencin, Studentska 2, 911 50 Trencin, Slovak Republic
[d] Faculty of Electrical Engineering and Communication, Brno University of Technology, Technicka 10, 616 00 Brno, Czech Republic
[e] Institute of Physics of Materials, Czech Academy of Sciences, Zizkova 22, 616 00 Brno, Czech Republic

ARTICLE INFO

Article history:
Received 15 February 2024
Accepted 4 June 2024
Available online xxx

Keywords:
$BaTiAl_6O_{12}$
Spark plasma sintering
Microstructure
Mechanical properties
Luminescence

ABSTRACT

In progressive particle or layered composites based on a combination of $BaTiO_3$ and Al_2O_3, serving as e.g. ceramic harvesters, new phases are formed during heat treatment. The dominant one is $BaTiAl_6O_{12}$. This study provides information about the microstructural, mechanical and optical properties of the $BaTiAl_6O_{12}$ ceramics. The evolution of the phases during the solid-state reaction synthesis of the $BaTiAl_6O_{12}$ was monitored. The fully dense samples prepared by spark plasma sintering had indentation Vickers hardness and indentation elastic modulus within ranges of 10.1–13.7 GPa and 132.0–187.0 GPa, depending on loading force. The three-point bending tests of the $BaTiAl_6O_{12}$ samples resulted in flexural strength of 129.9 MPa and fracture toughness of 1.8 MPa $m^{1/2}$. The sample showed blue broad-band emission under UV excitation due to the charge-transfer transition of the Ti^{4+} and defect sites. The $BaTiAl_6O_{12}$ evinced low permittivity (ε') = 16 and dielectric loss ($tan\,\delta$) <0.0003 at a frequency 1 kHz.

Caracterización microestructural, mecánica, eléctrica y óptica básica de cerámicas $BaTiAl_6O_{12}$

Palabras clave:
$BaTiAl_6O_{12}$
Spark plasma sintering
Microestructura
Propiedades mecánicas
Luminiscencia

RESUMEN

En los compuestos de partículas o capas progresivas basados en una combinación de $BaTiO_3$ y Al_2O_3, que sirven, por ejemplo, como capacitadores cerámicos, se forman fases nuevas durante el tratamiento térmico. La dominante es $BaTiAl_6O_{12}$. Este estudio proporciona información sobre las propiedades microestructurales, mecánicas y ópticas del cerámico $BaTiAl_6O_{12}$. Se monitorizó la evolución de las fases durante la síntesis por reacción en estado sólido de $BaTiAl_6O_{12}$. Las muestras totalmente densas preparadas mediante

* *Corresponding author.*
E-mail address: daniel.drdlik@ceitec.vutbr.cz (D. Drdlik).
https://doi.org/10.1016/j.bsecv.2024.06.002

Please cite this article in press as: D. Drdlik et al., Basic microstructural, mechanical, electrical and optical characterisation of $BaTiAl_6O_{12}$ ceramics, Bol. Soc. Esp. Cerám. Vidr. (2024), https://doi.org/10.1016/j.bsecv.2024.06.002

spark plasma sintering exhibieron una dureza Vickers por indentación y un módulo elástico por indentación entre 10,1-13,7 GPa y 132,0-187,0 GPa, respectivamente, dependiendo de la fuerza de carga aplicada. Los ensayos de flexión en tres puntos de las muestras de $BaTiAl_6O_{12}$ dieron como resultado una resistencia a la flexión de 129,9 MPa y una tenacidad a la fractura de 1,8 MPa $m^{1/2}$. La muestra presentó una emisión azul de banda ancha bajo excitación UV debido a la transición de transferencia de carga del Ti^{4+} y sitios defectuosos. El $BaTiAl_6O_{12}$ mostró una baja permitividad (ε') = 16 y una pérdida dieléctrica ($tan\,\delta$) < 0,0003 a una frecuencia de 1 kHz.

Introduction

Barium titanate ($BaTiO_3$) is one of the most important lead-free polycrystalline ceramic materials with attractive dielectric, ferroelectric and piezoelectric properties. It has found various applications in semiconductors, ultrasonic transducers, piezoelectric devices, pyroelectric detectors, etc. [1,2]. However, barium titanate shows relatively low mechanical characteristics compared with other ceramics. Therefore, the scientific efforts concentrate on reinforcing the barium titanate's microstructure with a mechanically hard phase to improve grain size, strength, hardness and fracture toughness. A typical example of such a hard phase is alumina (Al_2O_3).

From the microstructural point of view, the reinforcing alumina phase can be located in barium titanate as particles (grains) or in the form of layers. The particle composites are studied mainly in terms of improved hardness, Young's modulus, and gradually decreasing mean grain size with increasing content of alumina at acceptable piezoelectric properties [3–6]. On the other hand, the composites containing individual layers of barium titanate and alumina provide interesting results about the development of hardness and Young's modulus through the interface between layers, internal stresses, and crack propagation aiming at the final application as ceramic harvesters [7–9].

Although a few articles do not report the creation of new phases during the sintering process when barium titanate and alumina are mixed together [4,10,11], the majority of literary sources point to ongoing reactions to form new intermediate phases in particle composites [3,5,6,12–15] as well as reaction zones in layered composites [7–9]. Depending on the concentration of alumina, chosen fabrication technique, and the sintering conditions (temperature, heating rate, dwell time, pressure, etc.), the most frequently reported phases are $BaAl_2O_4$, $BaAl_{12}O_{20}$, $BaAl_{13.2}O_{20.8}$, $BaTi_2Al_3O_{10}$, $Ba_4Ti_{10}Al_2O_{27}$, and dominant $BaTiAl_6O_{12}$ [3,5,6,8,9,12–15]. Unfortunately, very little information is known about these phases, although they certainly have significant positive or negative effects on the final properties of the prepared composites.

For example, considering $BaTiAl_6O_{12}$ phase, Guha et al. [16] reported in 1976 petrographic and X-ray examinations of a sintered mixture containing stoichiometric composition $BaO:TiO_2:3Al_2O_3$ showing only one phase of $BaTiAl_6O_{12}$ stable at the solidus temperatures having tetragonal symmetry and densities of 3.84 g/cm^3 (measured) and 3.88 g/cm^3 (calculated). The authors also claimed that $BaTiAl_6O_{12}$ can be prepared by solid-state reaction from appropriate proportions of $BaTiO_3$ and Al_2O_3. Four years later, Guha [17] introduced a ternary diagram in the system $BaO–TiO_2–Al_2O_3$ at 1200 °C visualising the $BaTiAl_6O_{12}$ phase. Lately, the works of Cadée and Ijdo [18] and Fallon et al. [19] specified that $BaTiAl_6O_{12}$ was found to have orthorhombic symmetry instead of the reported tetragonal symmetry. Based on our best knowledge, we found only a recent work by de Pablos-Martin et al. [20] where the fluorescence of $BaTiAl_6O_{12}$, serving as a bonding layer between two sapphire substrates, was presented. Therefore, fundamental information about various properties of $BaTiAl_6O_{12}$ is still missing in the literature.

This study deals with $BaTiAl_6O_{12}$ ceramics as an important product arising in composites based on $BaTiO_3/Al_2O_3$. The properties of both Al_2O_3 and $BaTiO_3$ are thoroughly described in the literature, but information on the properties of $BaTiAl_6O_{12}$ is missing. Therefore, the effect of $BaTiAl_6O_{12}$ on the final properties of such composites is unclear. This paper aims to examine in detail the microstructural, mechanical, electrical and optical properties of $BaTiAl_6O_{12}$ and discuss them in relation to the materials from which it was synthesised. This will enable better understanding of characteristics of composite materials containing this phase.

Experimental

Preparation route

$BaTiAl_6O_{12}$ was prepared by mixing tetragonal barium titanate (Nanografi, Turkey) with alumina (Taimei, Japan) in an appropriate molar ratio to get the target stoichiometry after thermal treatment. The powder was milled in the planetary ball mill (Netzsch, Germany) for 30 min using deionised water as a solvent and 5 mm tetragonal zirconia balls as milling elements. The milled powder was dried for 24 h at 50 °C and then milled again in agate mortar.

The powder was uniaxially pressed in 30 mm die at 50 MPa. Then the pellet was cold isostatically pressed at 300 MPa followed by annealing at 800 °C to obtain a green body for high-temperature dilatometry. Spark plasma sintering (SPS, Dr. Sinter 615, Fuji, Japan) was used to consolidate the powder into a disc shape using a graphite die with a 30 mm diameter. The solid-state reaction took place at a sintering temperature of 1450 °C with 5 min dwell time using heating rate of

Please cite this article in press as: D. Drdlik et al., Basic microstructural, mechanical, electrical and optical characterisation of $BaTiAl_6O_{12}$ ceramics, Bol. Soc. Esp. Cerám. Vidr. (2024), https://doi.org/10.1016/j.bsecv.2024.06.002

100 °C/min, cooling rate of 50 °C/min and applied pressure of 50 MPa.

Analyses

High-temperature dilatometry (L70/1700, Linseis, Germany) was applied to identify temperature intervals of phase changes during sintering and the coefficient of thermal expansion (CTE). The thermal regimes were set at 1450 °C with 60 min dwell time (heating and cooling rates of 10 °C/min) and 500 °C without dwell (heating and cooling rates of 1 °C/min), respectively. The density of the sample was measured using the Archimedes method (ISO 18754). The phase composition of the sample was analysed using the SmartLab 3kW X-ray diffractometer (XRD, Rigaku, Japan). A piece from the sintered disc was cut, mounted onto the epoxy resin, ground, and polished on progressively finer diamond abrasives down to 1 μm. The polished surface was used for microstructural analysis using an SEM (Lyra 3 XMU, Tescan, Czech Republic) equipped with an EDS Ultimmax detector (Oxford Instruments, UK) and an EBSD Symmetry camera (Oxford Instruments, UK). The Aztec version 6.1 and Aztec Crystal version 3.1 (Oxford Instruments, UK) were used to analyse chemical composition and crystallography. A set of EBSD maps where the grain boundaries detection limit was set to an angle of 15° was used to obtain grain size distribution. The weighed area grain size frequency histogram was constructed based on more than 1750 grains. Mean grain size based on equivalent diameter and grain aspect ratio from major and minor fitted diameter was determined. Correction to the grain size to 3D was not applied.

Mechanical testing

To acquire indentation elastic modulus E_{IT} and Vickers hardness HV, the indentation techniques were used. Instrumented hardness was measured using a mechanical testing machine equipped with an indentation unit (Z2.5/ZHU0.2, Zwick/Roell, Germany) at 0.98–49.03 N loading. As multiple indentations can be performed on a single sample, more than ten valid measurements for statistical analysis were acquired for each load applied.

The Young's modulus E_{IET}, shear modulus G_{IET}, and consequently calculated Poisson's ratio were determined on the sintered disc of 30 mm in diameter and thickness of 1.6 mm by an impulse excitation technique using RFDA Professional (IMCE, Belgium) equipment at room temperature and air atmosphere. Elastic characteristics were determined from flexural and torsional resonant frequencies, disk geometry and density following the ASTM E1876 (ASTM C1259) standard [21,22].

All test specimens necessary for flexural strength and fracture toughness determination were cut from the sintered disk using a precise diamond saw Brillant 220 (ATM GmbH, Germany) and ground down to 10 μm diamond abrasive to eliminate cutting defects for the fracture toughness and down to ¼ μm for bending bars. The bending bars were also chamfered at the tensile side to eliminate corner stress concentration. The chevron notch was machined into the bars using a 0.15-mm-thick diamond cutting wheel.

Flexural strength was determined on test specimens loaded in the three-point bending configuration with a span of 8 mm. The nominal test specimen dimensions were predetermined by the disk thickness and were 2 mm × 2.5 mm × 10 mm. The flexural strength was determined from the fracture force when loaded using a universal electromechanical testing system (Instron 8862, UK) equipped with a load cell (HBM, Germany) of 500 N capacity. Similarly, using the same testing machine, the fracture toughness was determined on notched test specimens with a cross-section of 2.5 mm × 2 mm in size in a three-point bending configuration with a span of 10 mm. The chevron-notched beam method (CNB; ČSN EN 14425-3 for ceramics) was used to determine fracture toughness values $K_{Ic,cnb}$ calculated from the specimen's geometry, maximum of applied force and compliance function calculated via the slice method [23]. The details about this method and a comparison with the indentation can be found elsewhere [24,25].

Optical measurements

The photoluminescence excitation (PLE) and emission (PL) spectra were recorded at room temperature using a Fluorolog FL3-21 spectrometer (Horiba Jobin Yvon, France) in the backscattering configuration (front-face). The cw Xe-lamp (450 W) was used as an excitation source, and the luminescence signal was detected with a PPD-900 detector. The appropriate cut-off filters were used to eliminate the higher-order grating reflection artefacts in the PL spectra. The emission spectra were corrected for the spectrometer optics and the excitation lamp response. The sample surface was examined by X-ray photoelectron spectroscopy (XPS) using Nexsa G2 XPS Surface Analysis System (Thermo Scientific).

Electrical measurements

Dielectric properties were measured by Alpha-A High Performance Modular Measurement System (Novocontrol, Montabaur, Germany) in ZGS Active Sample Cell. The sample for this measurement was in the shape of a disc with a diameter of 12 mm and a thickness of 1 mm. A given amount of silver paste was applied to the sample. Then dielectric properties were measured at room temperature in a wide frequency range from 10 mHz to 1 MHz.

Results and discussion

Dilatometric measurements and XRD analysis

Fig. 1 shows the dilatometric record of the in situ conventionally sintered green body composed of barium titanate and alumina in the dilatometer. The dilatometric curve reveals that the compacted mixture is stable up to 1100 °C having no significant shrinkage. However, in the temperature range between 1100 °C and 1450 °C, sintering shrinkage occurs accompanied by two significant events associated with phase changes as a result of the solid-state reaction. The phase transformations begin at 1154 °C and 1314 °C, respectively. To explore phase evolution during sintering, three samples were

Please cite this article in press as: D. Drdlik et al., Basic microstructural, mechanical, electrical and optical characterisation of $BaTiAl_6O_{12}$ ceramics, Bol. Soc. Esp. Cerám. Vidr. (2024), https://doi.org/10.1016/j.bsecv.2024.06.002

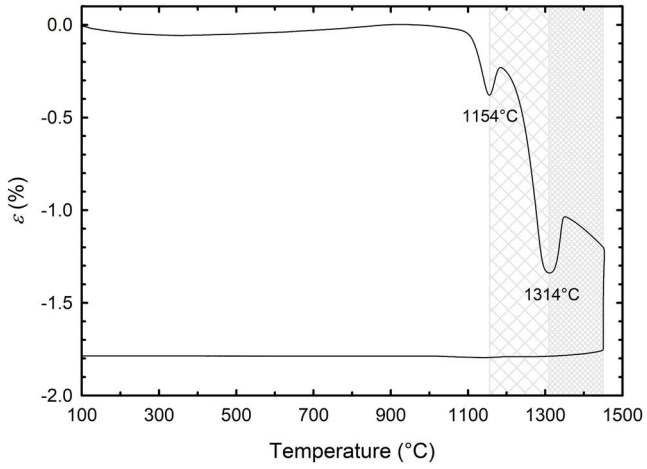

Fig. 1 – Sintering shrinkage of the conventionally sintered mixture of tetragonal barium titanate and alumina.

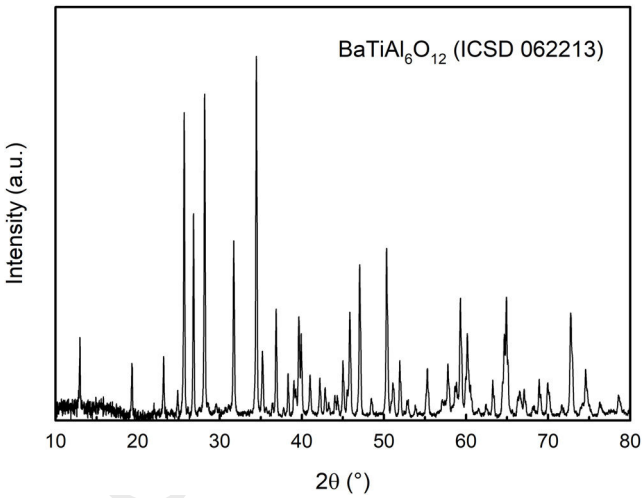

Fig. 3 – X-ray diffraction pattern of sample sintered using SPS.

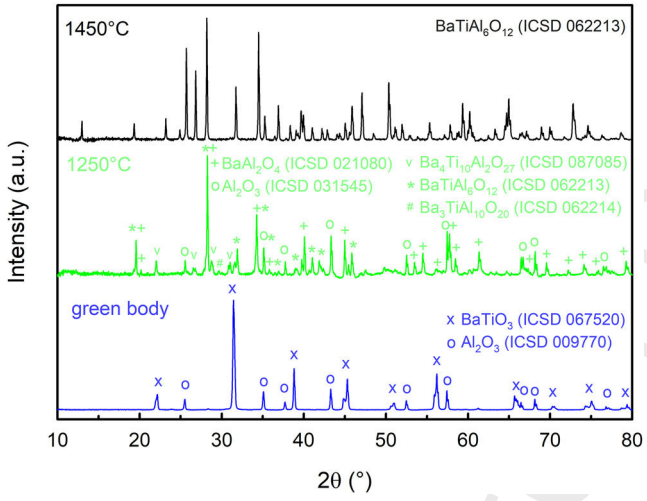

Fig. 2 – X-ray diffraction patterns of conventionally sintered samples at 800 °C, 1250 °C and 1450 °C.

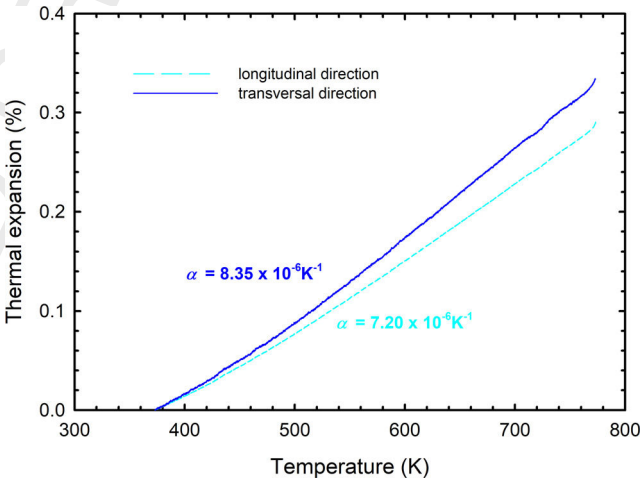

Fig. 4 – Cooling parts of dilatometric curves serving for calculation of CTE in the longitudinal and transversal orientation of the sample.

analysed using XRD. The first one was the green body, the second one was sintered at 1250 °C (in the region after the first phase transformation occurrence, see Fig. 1) and the third one was sintered at 1450 °C (in the region after the second phase transformation). The XRD analyses, given in Fig. 2, show the transformation of two distinct phases ($BaTiO_3$ and Al_2O_3) into $BaAl_2O_4$, $BaTiAl_6O_{12}$, $Ba_4Ti_{10}Al_2O_{27}$, $Ba_3TiAl_{10}O_{20}$ and Al_2O_3 at 1250 °C. The major phase was unreacted alumina (48 wt.%), followed by $BaAl_2O_4$ (27 wt.%) and other minor phases. Higher temperature (1450 °C) resulted in the transformation of all these phases to a single $BaTiAl_6O_{12}$ phase.

However, Fig. 1 also shows quite a small sintering shrinkage of ~1.8%, although the relative density of the green body was moderately high ($\rho_{g.b.}$ = 59.6%), indicating a low final density of the conventionally pressure-less sintered sample. It was confirmed by density measurement, reaching a value of 77.2%. From the practical point of view, we decided to use non-conventional sintering (SPS) at the same temperature with applied pressure to get a fully dense sample. The spark plasma sintered sample reached a relative density of 99.5%. The XRD analysis of the SPS sample is given in Fig. 3. The X-ray diffraction pattern comprises peaks of the $BaTiAl_6O_{12}$ phase.

Fig. 4 shows the cooling parts of dilatometric curves of sintered SPS samples for the determination of CTE. The CTE was calculated for the sample's transversal (plane of the disc base) and longitudinal (direction of applied pressure during SPS) orientation. The calculated values of CTEs in the temperature range between 100 °C and 500 °C were $8.35 \times 10^{-6}\,K^{-1}$ and $7.20 \times 10^{-6}\,K^{-1}$ for transversal and longitudinal orientation, respectively. The calculated CTEs of the $BaTiAl_6O_{12}$ phase are closer to the CTE of alumina ($8 \times 10^{-6}\,K^{-1}$ [26]) rather than of barium titanate ($11 \times 10^{-6}\,K^{-1}$ [8,27]). Calculated CTE values and different slopes of dilatometric curves may seem to indicate anisotropy of the coefficient of thermal expansion of $BaTiAl_6O_{12}$. The anisotropy was found not in the grain orientation but in the aspect ratio only (discussed further). However,

Please cite this article in press as: D. Drdlik et al., Basic microstructural, mechanical, electrical and optical characterisation of $BaTiAl_6O_{12}$ ceramics, Bol. Soc. Esp. Cerám. Vidr. (2024), https://doi.org/10.1016/j.bsecv.2024.06.002

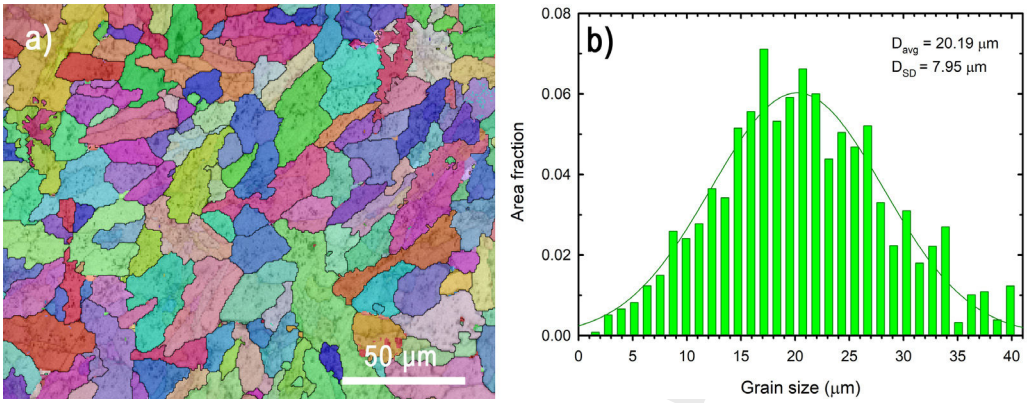

Fig. 5 – Images of (a) EBSD map and (b) grain size distribution of sample sintered using SPS.

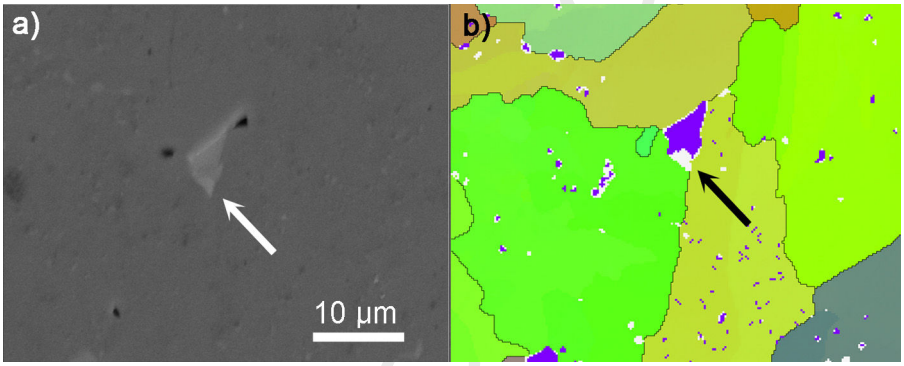

Fig. 6 – SEM images (a) and corresponding EBSD map (b) of sample sintered using SPS.

the generally known variance of CTE values must also be considered.

Microstructure

The microstructure visualised using the EBSD detector in SEM is shown in Fig. 5a. The image shows rather elongated grains with different crystallographic orientations of the orthorhombic lattice. The grain growth direction preference may have been caused by the applied pressure during the sintering process. The aspect ratio of the fitted major and minor ellipse diameter is equal to 2.1. Grain orientation anisotropy was not detected based on the EBSD data. The area-weighted grain size distribution is plotted in Fig. 5b. The mean grain size of the SPS sample determined using the distribution function was 20.19 µm.

The EBDS analysis also revealed the existence of the secondary phase. This phase can be seen due to phase contrast in the SEM image in Fig. 6a and, at the same time, also on the corresponding EBDS map. The phase (purple area in Fig. 6b) was identified as monoclinic $Ba_3TiAl_{10}O_{20}$ localised mainly in the triple points of the $BaTiAl_6O_{12}$ phase. It was represented in the amount of 2.5% of all the phases analysed by EBDS. Therefore, it was not detected by XRD due to the resolution limit of the instrument. However, the bright grain in Fig. 6a contains an even brighter area marked by the white arrow in the SEM image and the black arrow in the EBDS map as not identified area. It is believed that they are the transition reaction products of incomplete transformation on $BaTiAl_6O_{12}$. Although the minor phases were analysed, we assume that their small amounts do not substantially affect the final properties of the $BaTiAl_6O_{12}$.

Mechanical properties

The indentation at various loading levels was conducted to obtain a set of data revealing information about the size effect of the $BaTiAl_6O_{12}$. The dependence is shown in Fig. 7 for both the Vickers hardness calculated from measured indentation depth and calculated indentation elastic modulus determined from the unloading part of loading curves. Both dependencies exhibit typical shapes where approximately for loads above 10 N a plateau can be identified and the hardness of the $BaTiAl_6O_{12}$ can be estimated at the level of 10 GPa. The indentation elastic modulus ranked between 187 GPa for HV0.1 and 132 GPa for HV5. The load of HV5 (49.05 N) and above led to the formation of significantly large cracks but the value of hardness could not be affected by this phenomenon known for brittle materials [28].

The elastic properties obtained by the impulse excitation technique showed slightly higher values of Young's modulus than the average in indentation. The calculated value from resonance frequencies was 179.4 ± 0.08 GPa which corresponds rather with the indentation elastic modulus obtained at lower loads applied. This finding is in good correlation with the fact that E_{IET} generally provides higher and more precious

Please cite this article in press as: D. Drdlik et al., Basic microstructural, mechanical, electrical and optical characterisation of $BaTiAl_6O_{12}$ ceramics, Bol. Soc. Esp. Cerám. Vidr. (2024), https://doi.org/10.1016/j.bsecv.2024.06.002

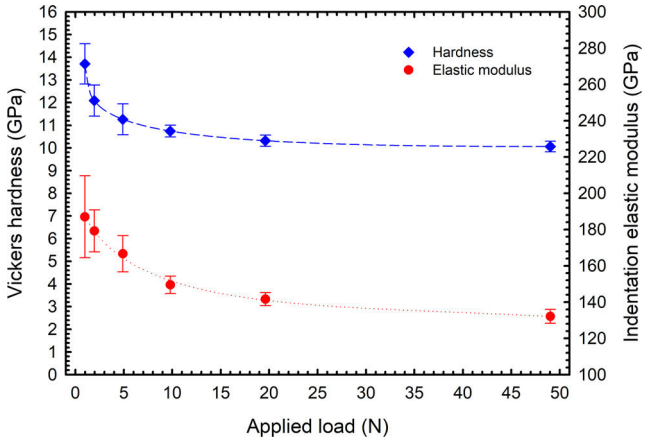

Fig. 7 – Dependence of Vickers hardness and indentation elastic modulus on the applied load.

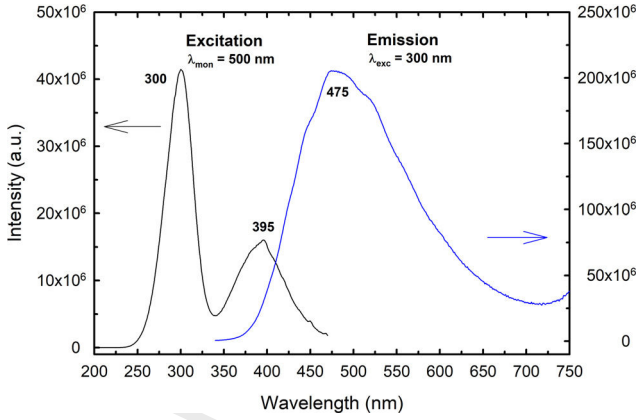

Fig. 9 – The excitation and emission spectrum of $BaTiAl_6O_{12}$ ceramics recorded at room temperature.

values than methods based on mechanical deformation and is rather comparable with nanoindentation [29]. The E_{IET} also allows the determination of shear modulus and the calculation of Poisson's ratio to be 69.5 ± 0.05 GPa and 0.29 ± 0.001, respectively. Compared with the $BaTiO_3$, elastic properties are slightly higher but deeply below typical values for alumina [30,31].

The flexural strength determined by three-point bending was 129.9 ± 4.57 MPa, which is approximately 30% higher than typical maximal values for $BaTiO_3$ laying on the level of 100 MPa [30]. The fracture toughness of the $BaTiO_3$ is mostly determined by the indentation technique; however, some works also use standard approaches, resulting in the values oscillating around 1 MPa $m^{1/2}$ [29,32]. To compare with the $BaTiAl_6O_{12}$, the measured value was 1.8 ± 0.15 MPa $m^{1/2}$, i.e., 80% higher; however, not reaching the typical value 3.6 MPa $m^{1/2}$ for alumina [33]. Generally, it can be stated that $BaTiAl_6O_{12}$ exhibits overall better mechanical properties than $BaTiO_3$; therefore, it will be beneficial when formed at the interfaces with Al_2O_3. The typical fracture surface is presented in Fig. 8, showing transgranular fracture mode on the backscattered electron mode of SEM images. The observed transgranular fracture mode indicates a strong boundary strength of adjacent grains [34]. The detailed view (see Fig. 8c) shows that the secondary phase (white grain of $Ba_3TiAl_{10}O_{20}$) did not change the overall fracture morphology.

Optical properties

The crystal structure of $BaTiAl_6O_{12}$, reported by Fallon et al. [19], consists of two types of octahedra with mixed Ti and Al occupancy and tetrahedra (AlO_4) forming a three-dimensional framework with tunnels containing barium ions. From these constituents, only the Ti-oxygen polyhedron can absorb ultraviolet light due to charge-transfer transitions as known for a large number of hosts [35,36]. The tetrahedral titanate group (TiO_4) absorbs only at wavelengths shorter than 250 nm [36], while the octahedral titanate groups (TiO_6) absorbs at longer wavelengths. Because Ti occupies only octahedral sites in $BaTiAl_6O_{12}$, absorption at longer wavelengths than 250 nm is expected.

Since various titanium oxidation states (mainly Ti^{4+}/Ti^{3+}) in oxide hosts may contribute to the luminescence, the sample surface was examined by XPS (figure not shown). The two prominent Ti 2p peaks originating from Ti $2p_{1/2}$ at 464.6 eV and $2p_{3/2}$ at 458.6 eV were observed in the XPS spectrum corresponding to the Ti^{4+}-ion profile. This suggests that almost no or only negligible reduction of Ti^{4+} to Ti^{3+} occurs, and the Ti ions maintain the stable valence state of 4+.

The excitation (PLE) and emission (PL) spectra of $BaTiAl_6O_{12}$ ceramic are presented in Fig. 9. The PLE spectrum was recorded under the monitoring of the emission wavelength at 475 nm and 500 nm, respectively. The spectrum consists of two broad bands, the first most intensive band in the wavelength

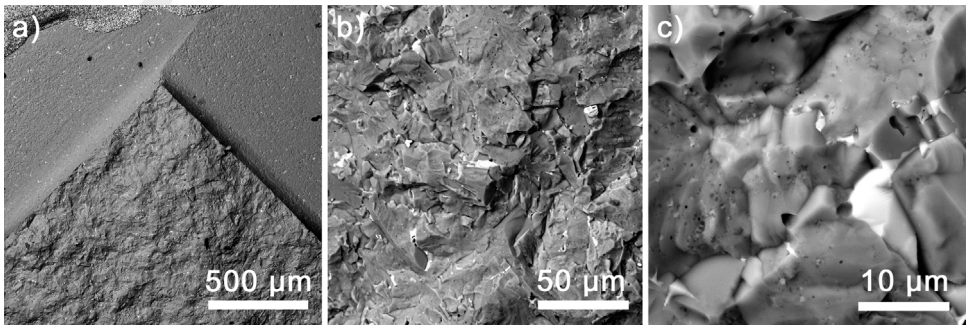

Fig. 8 – Typical example of the fracture surface of CNB specimen with increasing magnification from left to right.

Please cite this article in press as: D. Drdlik et al., Basic microstructural, mechanical, electrical and optical characterisation of $BaTiAl_6O_{12}$ ceramics, Bol. Soc. Esp. Cerám. Vidr. (2024), https://doi.org/10.1016/j.bsecv.2024.06.002

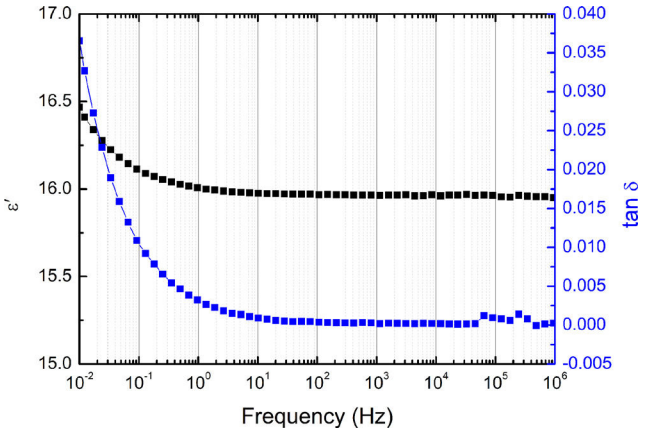

Fig. 10 – Real part of permittivity (ε') and dielectric loss ($tan\,\delta$) vs frequency at room temperature.

range of 250–340 nm centred at about 300 nm, and the second one in the range of 340–500 nm with a maximum at 395 nm. No absorption band at around 500 nm, typical for the Ti^{3+} ions, was observed in excitation spectra. The excitation at 300 nm corresponds to Ti^{4+}–O^{2-} charge-transfer transition (CT) from the 2p orbital of O^{2-} into the 3*d* orbital of Ti^{4+}, which is common for titanates and Ti-doped compounds [37–41]. When the ceramic was excited at this wavelength, the broad-band emission ranging between 360 and 700 nm and centred at 475 nm was observed. This emission can be attributed to the charge-transfer transition of the Ti^{4+} with the following mechanism [39–41]: $Ti^{4+} + h\upsilon_{exc} \rightarrow Ti^{3+} + h^{+} \rightarrow (Ti^{4+})^{*} \rightarrow Ti^{4+} + h\upsilon_{lum}$. In this mechanism, an electron from the valence band is transferred to Ti^{4+} ion with the creation of Ti^{3+} and a hole in the valence band (strongly coupled electron–hole system Ti^{3+}–O^{-}), resulting in Ti^{3+} ion in the electronic excited state. Subsequently, the interaction between excited (3d) electron and lattice results in the Stokes shift and finally, this excitation is radiatively annihilated, emitting the photon around 475 nm.

The origin of the second absorption band centred at 395 nm in the PLE spectrum is not unequivocally clear, but this band is probably associated with defect sites in the structure. The excitation of $BaTiAl_6O_{12}$ ceramic in this wavelength range also leads to the visible emission between 400 and 650 nm (a bit blue shifted with a maximum at 460 nm); however, new less intensive broad-band emission appeared in the NIR range of 720–850 nm and centred at 775 nm. This implies that various defect sites may also contribute to overall luminescence in $BaTiAl_6O_{12}$.

Electrical properties

A real part of permittivity (ε') and the dielectric loss ($tan\,\delta$) of $BaTiAl_6O_{12}$ as a function of frequency, measured at room temperature, are shown in Fig. 10. The sample evinced very low permittivity (ε') = 16 and dielectric loss ($tan\,\delta$) <0.0003 at a frequency 1 kHz. At a frequency range 10 mHz to 1 MHz, the ε' evinces the highest value of 16.5 at a frequency of 10 mHz and smoothly decreases to approximately 16, up to a frequency of 1 Hz. Then ε' is approximately constant at 16 up to a frequency of 1 MHz. The $tan\,\delta$ shows similar behaviour. At the lowest frequency of 10 mHz, the sample evinced the highest loss about 0.035. Then $tan\,\delta$ drops sharply to 0.003 for a frequency of 1 Hz. Further, the losses decrease gradually to a minimal value of approximately 0.0001 with an increasing frequency.

Conclusions

$BaTiAl_6O_{12}$ was successfully prepared during the solid-state reaction of the tetragonal barium titanate and alumina mixture in an appropriate molar ratio. During thermal treatment, two events of phase changes were determined and analysed. The applied spark plasma sintering resulted in dense samples reaching the relative density of 99.5%. Coefficients of thermal expansion were calculated from the dilatometric measurements ranging from 7.20 to 8.35 × 10^{-6} K^{-1} in dependence on the sample orientation. The EBSD analysis showed elongated grains (mean grain size of 20.19 μm) with different crystallographic orientations of the orthorhombic lattice and 2.5% of monoclinic $Ba_3TiAl_{10}O_{20}$ phase localised mainly in the triple points of the $BaTiAl_6O_{12}$ phase. The Vickers hardness and indentation modulus were force dependent and for loads between HV0.1 and HV5 ranged between 13.7 GPa and 10.1 GPa for the Vickers hardness and between 187 GPa and 132 GPa for the indentation modulus. Young's modulus calculated from resonance frequencies was 179 GPa. The flexural strength and fracture toughness of $BaTiAl_6O_{12}$ determined by three-point bending were 129.9 ± 4.57 MPa and 1.8 ± 0.15 MPa $m^{1/2}$, respectively. The fractographic analysis of the fracture surfaces revealed transgranular fracture mode. In the case of optical properties, the blue broad-band emission under UV excitation was observed in $BaTiAl_6O_{12}$ ceramics, which is due to the charge-transfer transition of the Ti^{4+} and defect sites. The measurement of electrical properties at room temperature showed low permittivity (ε') = 16 and dielectric loss ($tan\,\delta$) <0.0003 at a frequency 1 kHz.

Data availability statement

The datasets generated during and/or analysed during the current study are available in the repository (https://doi.org/10.5281/zenodo.10609604).

Conflict of interests

The authors declare that they have no known competing financial interests or personal relationships that could have appeared to influence the work reported in this paper.

Acknowledgements

Financial support of the Czech Science Foundation under project no. 21-24805S is gratefully acknowledged. This publication was supported by the project "Mechanical Engineering of Biological and Bio-inspired Systems", funded as project No. CZ.02.01.01/00/22_008/0004634 by Programme Johannes Amos Commenius, call Excellent Research. This work was also supported by the Slovak grant agency under the grant

VEGA 1/0476/22. The authors would like to thank Dr. Kamalan Mosas for recording the XPS spectra and helpful discussion. We acknowledge CzechNanoLab Research Infrastructure supported by MEYS CR (LM2023051).

REFERENCES

[1] B. Ertuğ, The overview of the electrical properties of barium titanate, Am. J. Eng. Res. 2 (2013) 1–7.
[2] M.M. Vijatović, J.D. Bobić, B.D. Stojanović, History and challenges of barium titanate: part II, Sci. Sinter. 40 (2008) 235–244, http://dx.doi.org/10.2298/SOS0803235V.
[3] S. Jiansirisomboon, A. Watcharapasorn, T. Tunkasiri, Effects of Al_2O_3 nano-particulates addition on barium titanate ceramics, Chiang Mai J. Sci. 33 (2006) 175–182.
[4] S. Jiansirisomboon, A. Watcharapasorn, Effects of alumina nano-particulates addition on mechanical and electrical properties of barium titanate ceramics, Curr. Appl. Phys. 8 (2008) 48–52, http://dx.doi.org/10.1016/j.cap.2007.04.008.
[5] J.G. Fisher, B.-K. Lee, A. Brancquart, S.-Y. Choi, S.-J.L. Kang, Effect of Al_2O_3 dopant on abnormal grain growth in $BaTiO_3$, J. Eur. Ceram. Soc. 25 (2005) 2033–2036, http://dx.doi.org/10.1016/j.jeurceramsoc.2005.03.065.
[6] J.G. Fisher, B.-K. Lee, S.-Y. Choi, S.-M. Wang, S.-J.L. Kang, Inhibition of abnormal grain growth in $BaTiO_3$ by addition of Al_2O_3, J. Eur. Ceram. Soc. 26 (2006) 1619–1628, http://dx.doi.org/10.1016/j.jeurceramsoc.2005.03.234.
[7] Z. Chlup, D. Drdlík, M. Fides, A. Kovalčíková, H. Hadraba, Properties of $BaTiO_3/Al_2O_3$ laminate structure by nanoindentation, Procedia Struct. Integr. 23 (2019) 499–504, http://dx.doi.org/10.1016/j.prostr.2020.01.135.
[8] H. Hadraba, Z. Chlup, D. Drdlík, F. Šiška, Characterisation of mechanical and fracture behaviour of $Al_2O_3/ZrO_2/BaTiO_3$ laminate by indentation, J. Eur. Ceram. Soc. 40 (2020) 4799–4807, http://dx.doi.org/10.1016/j.jeurceramsoc.2020.04.024.
[9] P. Tofel, Z. Machu, Z. Chlup, H. Hadraba, D. Drdlik, O. Sevecek, Z. Majer, V. Holcman, Z. Hadas, Novel layered architecture based on $Al_2O_3/ZrO_2/BaTiO_3$ for SMART piezoceramic electromechanical converters, Eur. Phys. J. Spec. Top. 228 (2019) 1575–1588, http://dx.doi.org/10.1140/epjst/e2019-800153-0.
[10] A.I. Ali, M.M. Hassan, G. Goda Mohammed, H.Y. Abdel El-Hamid, H. Awad, Preparation, structural and dielectric properties of nanocomposite $Al_2O_3/BaTiO_3$ for multilayer ceramic capacitors applications, J. Mater. Res. Technol. 18 (2022) 2083–2092, http://dx.doi.org/10.1016/j.jmrt.2022.03.041.
[11] C. Yu, S. Wang, K. Zhang, M. Li, H. Gao, J. Zhang, H. Yang, L. Hu, A.V. Jagadeesha, D. Li, Visible-light-enhanced photocatalytic activity of $BaTiO_3/\gamma$-Al_2O_3 composite photocatalysts for photodegradation of tetracycline hydrochloride, Opt. Mater. 135 (2023) 113364, http://dx.doi.org/10.1016/j.optmat.2022.113364.
[12] S. Rattanachan, Y. Miyashita, Y. Mutoh, Microstructure and fracture toughness of a spark plasma sintered Al_2O_3-based composite with $BaTiO_3$ particulates, J. Eur. Ceram. Soc. 23 (2003) 1269–1276, http://dx.doi.org/10.1016/S0955-2219(02)00294-7.
[13] S. Rattanachan, Y. Miyashita, Y. Mutoh, Effect of polarization on fracture toughness of $BaTiO_3/Al_2O_3$ composites, J. Eur. Ceram. Soc. 24 (2004) 775–783, http://dx.doi.org/10.1016/S0955-2219(03)00319-4.
[14] S. Rattanachan, Y. Miyashita, Y. Mutoh, Fatigue behavior of Al_2O_3-based composite with $BaTiO_3$ piezoelectric phase, Int. J. Fatigue 28 (2006) 1413–1419, http://dx.doi.org/10.1016/j.ijfatigue.2006.02.022.
[15] X.M. Chen, B. Yang, A new approach for toughening of ceramics, Mater. Lett. 33 (1997) 237–240, http://dx.doi.org/10.1016/S0167-577X(97)00107-9.
[16] J.P. Guha, D. Kolar, B. Volavšek, Preparation and characterization of new ternary compounds in the system $BaO–TiO_2–Al_2O_3$, J. Solid State Chem. 16 (1976) 49–54, http://dx.doi.org/10.1016/0022-4596(76)90006-2.
[17] J.P. Guha, Subsolidus equilibria in the system $BaO–TiO_2–Al_2O_3$, J. Solid State Chem. 34 (1980) 17–22, http://dx.doi.org/10.1016/0022-4596(80)90397-7.
[18] M.C. Cadée, D.J.W. Ijdo, Revised crystal data for $BaTiAl_6O_{12}$ and isomorphs, Mater. Res. Bull. 17 (1982) 481–484, http://dx.doi.org/10.1016/0025-5408(82)90103-9.
[19] G.D. Fallon, B.M. Gatehouse, P.J. Wright, Single crystal structure determinations of $BaTiAl_6O_{12}$ and $Ba_3TiAl_{10}O_{20}$, J. Solid State Chem. 60 (1985) 203–208, http://dx.doi.org/10.1016/0022-4596(85)90113-6.
[20] A. de Pablos-Martin, S. Tismer, G. Benndorf, M. Mittag, M. Lorenz, M. Grundmann, T. Höche, Laser soldering of sapphire substrates using a $BaTiAl_6O_{12}$ thin-film glass sealant, Opt. Laser Technol. 81 (2016) 153–161, http://dx.doi.org/10.1016/j.optlastec.2016.02.008.
[21] Standard Test Method for Dynamic Young's Modulus, Shear Modulus, and Poisson's Ratio by Impulse Excitation of Vibration, ASTM International, West Conshohocken, PA, 2022, http://dx.doi.org/10.1520/E1876-22.
[22] Standard Test Method for Dynamic Young's Modulus, Shear Modulus, and Poisson's Ratio for Advanced Ceramics by Impulse Excitation of Vibration, ASTM International, West Conshohocken, PA, 2021, http://dx.doi.org/10.1520/C1259-21.
[23] J.I. Bluhm, Slice synthesis of a three dimensional "work of fracture" specimen, Eng. Fract. Mech. 7 (1975) 593–604, http://dx.doi.org/10.1016/0013-7944(75)90059-4.
[24] Z. Chlup, D.N. Boccaccini, C. Leonelli, M. Romagnoli, A.R. Boccaccini, Fracture behaviour of refractory ceramics after cyclic thermal shock, Ceram. -Silik. 50 (2006) 245–250.
[25] P. Tatarko, S. Grasso, H. Porwal, Z. Chlup, R. Saggar, I. Dlouhý, M.J. Reece, Boron nitride nanotubes as a reinforcement for brittle matrices, J. Eur. Ceram. Soc. 34 (2014) 3339–3349, http://dx.doi.org/10.1016/j.jeurceramsoc.2014.03.028.
[26] D. Kuscer, I. Bantan, M. Hrovat, B. Malič, The microstructure, coefficient of thermal expansion and flexural strength of cordierite ceramics prepared from alumina with different particle sizes, J. Eur. Ceram Soc. 37 (2017) 739–746, http://dx.doi.org/10.1016/j.jeurceramsoc.2016.08.032.
[27] Y. He, Heat capacity, thermal conductivity, and thermal expansion of barium titanate-based ceramics, Thermochim. Acta 419 (2004) 135–141, http://dx.doi.org/10.1016/j.tca.2004.02.008.
[28] J.L. Wang, D.J. Ma, L. Sun, The influence of crack forms on indentation hardness test results for ceramic materials, J. Mater. Sci. 50 (2015) 6096–6102, http://dx.doi.org/10.1007/s10853-015-9162-2.
[29] M. Radovic, E. Lara-Curzio, L. Riester, Comparison of different experimental techniques for determination of elastic properties of solids, Mater. Sci. Eng.: A 368 (2004) 56–70, http://dx.doi.org/10.1016/j.msea.2003.09.080.
[30] J.M. Blamey, T.V. Parry, Strength and toughness of barium titanate ceramics, J. Mater. Sci. 28 (1993) 4988–4993, http://dx.doi.org/10.1007/BF00361166.
[31] Z. Chlup, H. Hadraba, L. Slabáková, D. Drdlík, I. Dlouhý, Fracture behaviour of alumina and zirconia thin layered laminate, J. Eur. Ceram. Soc. 32 (2012) 2057–2061, http://dx.doi.org/10.1016/j.jeurceramsoc.2011.09.006.
[32] Z. Chlup, D. Drdlík, H. Hadraba, O. Ševeček, F. Šiška, J. Erhart, K. Maca, Temperature effect on elastic and fracture behaviour of lead-free piezoceramic $BaTiO_3$, J. Eur. Ceram.

Please cite this article in press as: D. Drdlik et al., Basic microstructural, mechanical, electrical and optical characterisation of $BaTiAl_6O_{12}$ ceramics, Bol. Soc. Esp. Cerám. Vidr. (2024), https://doi.org/10.1016/j.bsecv.2024.06.002

Soc. 43 (2023) 1509–1522, http://dx.doi.org/10.1016/j.jeurceramsoc.2022.11.030.
[33] J. Kübler, Fracture toughness of ceramics using the SEVNB method a joint VAMSA/ESIS Round Robin, in: R.C. Bradt, D. Munz, M. Sakai, V.Y. Shevchenko, K. White (Eds.), Fracture Mechanics of Ceramics: Volume 13. Crack-Microstructure Interaction, R-Curve Behavior, Environmental Effects in Fracture, and Standardization, Springer, Boston, MA, US, 2002, pp. 437–445.
[34] G.D. Quinn, Fractography of Ceramics and Glasses, National Institute of Standards and Technology, U.S. Department of Commerce, 2016.
[35] M.C. Cadée, D.J.W. Ijdo, G. Blasse, Crystal structure and luminescence of compounds $A_3BC_{10}O_{20}$, J. Solid State Chem. 41 (1982) 39–43, http://dx.doi.org/10.1016/0022-4596(82)90031-7.
[36] G. Blasse, The Luminescence of Closed-shell Transition-metal Complexes. New Developments, Luminescence and Energy Transfer, Springer Berlin Heidelberg, Berlin, Heidelberg, 1980, pp. 1–41.
[37] Y. Li, Y. Wang, X. Xu, G. Yu, N. Wang, Electronic structures and Pr^{3+} photoluminescence characteristics in fresnoite, Sr-frenoite, and Ge-frenoite, J. Am. Ceram. Soc. 94 (2011) 496–500, http://dx.doi.org/10.1111/j.1551-2916.2010.04108.x.
[38] P.S. Page, B.S. Dhabekar, B.C. Bhatt, A.R. Dhoble, S.V. Godbole, Role of Ti^{4+} in the luminescence process of Al_2O_3:Si,Ti, J. Lumin. 130 (2010) 882–887, http://dx.doi.org/10.1016/j.jlumin.2009.12.029.
[39] V.B. Mikhailik, P.C.F. Di Stefano, S. Henry, H. Kraus, A. Lynch, V. Tsybulskyi, M.A. Verdier, Studies of concentration dependences in the luminescence of Ti-doped Al_2O_3, J. Appl. Phys. 109 (2011), http://dx.doi.org/10.1063/1.3552943.
[40] T. Sato, M. Shirai, K. Tanaka, Y. Kawabe, E. Hanamura, Strong blue emission from Ti-doped $MgAl_2O_4$ crystals, J. Lumin. 114 (2005) 155–161, http://dx.doi.org/10.1016/j.jlumin.2004.12.016.
[41] A. Jouini, H. Sato, A. Yoshikawa, T. Fukuda, G. Boulon, G. Panczer, K. Kato, E. Hanamura, Ti-doped $MgAl_2O_4$ spinel single crystals grown by the micro-pulling-down method for laser application: growth and strong visible blue emission, J. Mater. Res. 21 (2006) 2337–2344, http://dx.doi.org/10.1557/jmr.2006.0280.

Please cite this article in press as: D. Drdlik et al., Basic microstructural, mechanical, electrical and optical characterisation of $BaTiAl_6O_{12}$ ceramics, Bol. Soc. Esp. Cerám. Vidr. (2024), https://doi.org/10.1016/j.bsecv.2024.06.002